Evaluation of the Empirical Scaling Factor of Joule Heating Rates in TIE-GCM with EISCAT Measurements

Florian Günzkofer[1], Huixin Liu[2], Gunter Stober[3], Dimitry Pokhotelov[4], and Claudia Borries[1]

[1]Institute for Solar-Terrestrial Physics, German Aerospace Center (DLR), Neustrelitz, Germany
[2]Department of Earth and Planetary Sciences, Kyushu University, Fukuoka, Japan
[3]Institute of Applied Physics & Oeschger Center for Climate Change Research, Microwave Physics, University of Bern, Bern, Switzerland
[4]Institute of Physics, University of Greifswald, Greifswald, Germany

Key Points:

- The TIE-GCM model applies an empirical scaling factor of 1.5 to compensate the general underestimation of Joule heating rates.
- Joule heating rates from 2220 h of EISCAT measurements are compared to TIE-GCM runs driven with the *Heelis* and *Weimer* convection models.
- The required scaling factor varies significantly with the Kp index, the Kan-Lee merging electric field, and the magnetic local time.

Corresponding author: Florian Günzkofer, florian.guenzkofer@dlr.de

Corresponding author: Huixin Liu, liu.huixin.295@m.kyushu-u.ac.jp

Abstract

Joule heating is one of the main energy inputs into the thermosphere-ionosphere system. Precise modeling of this process is essential for any space weather application. Existing ionosphere models tend to underestimate the actual Joule heating rate quite significantly. The Thermosphere-Ionosphere-Electrodynamics General-Circulation-Model applies an empirical scaling factor of 1.5 for compensation. We calculate vertical profiles of Joule heating rates from approximately 2220 h of measurements with the EISCAT incoherent scatter radar and the corresponding model runs. We investigate model runs with the plasma convection driven by both the *Heelis* and the *Weimer* model. The required scaling of the Joule heating profiles is determined with respect to the Kp index, the Kan-Lee merging electric field E_{KL}, and the magnetic local time. Though the default scaling factor of 1.5 appears to be adequate on average, we find that the required scaling varies strongly with all three parameters ranging from 0.46 to $\sim$ 20 at geomagnetically disturbed and quiet times, respectively. Furthermore, the required scaling is significantly different in runs driven by the *Heelis* and *Weimer* model. Adjusting the scaling factor with respect to the Kp index, E_{KL}, the magnetic local time, and the choice of convection model would reduce the difference between measurement and model results.

Plain Language Summary

The vast majority of the energy input to the Earth system originates from the sun. This includes the absorption of various types of radiation, e.g. ultraviolet radiation in the ozone layer or visible light and infrared radiation at the surface. In the ionosphere above about 80 km altitude, the absorption of extreme ultraviolet radiation and soft X-rays plays a major role. However, other processes also contribute significantly to the heating of this region, e.g. the dissipation of electric currents, also known as Joule heating. Especially during solar storms, which can have potentially disastrous effects on satellites and power grids, Joule heating plays a crucial role. Accurate modeling, and therefore also prediction, of Joule heating is not possible at the moment since ionosphere models have to scale the Joule heating empirically to fit the actual values. We investigate how the required scaling changes under different geophysical conditions.

1 Introduction

Ionospheric heating is caused by several different mechanisms and their respective impacts vary strongly with geomagnetic activity and latitude. Ionospheric modeling and space weather prediction require understanding and accurately describing these processes such as e.g. energetic particle precipitation or absorption of extreme ultraviolet and soft X-ray radiation. At high latitudes, especially during geomagnetic active periods, the *Joule heating* due to dissipation of ionospheric currents is of major importance for the ionosphere-thermosphere system. The local Joule heating rate is defined as

$$q_J = \mathbf{j} \cdot \mathbf{E} \tag{1}$$

with the current density $\mathbf{j}$ and the electric field $\mathbf{E}$.

At high latitudes, ionospheric currents are induced by the polar plasma convection, which results from the interaction of the Earth's magnetic field and the interplanetary magnetic field (IMF) carried by the solar wind (e.g. Baumjohann & Treumann, 1996; Kelley, 2009; Schunk & Nagy, 2009). The convection pattern gives rise to an electric field $\mathbf{E}_\perp$ perpendicular to the nearly vertical magnetic field lines. In this situation, two types of currents can be distinguished: Pedersen currents $\mathbf{j}_P$ ($\parallel \mathbf{E}_\perp$) parallel to the electric field and Hall currents $\mathbf{j}_H$ ($\parallel \mathbf{E}_\perp \times \mathbf{B}$) perpendicular to both the electric field and the magnetic field lines. From Eq. 1, it can be seen that only Pedersen currents contribute to the Joule heating rate. Introducing the Pedersen conductivity σ_P, the Pedersen current

can be written as $\mathbf{j}_P = \sigma_P \mathbf{E}_\perp$. Including the neutral dynamo effect due to the neutral wind $\mathbf{u}(z)$, the altitude-dependent Joule heating rate is

$$q_J(z) = \sigma_P(z) \left(\mathbf{E}_\perp + \mathbf{u}(z) \times \mathbf{B}(z)\right)^2 \qquad [\mathrm{Wm}^{-3}]. \tag{2}$$

Integration of Eq. 2 gives the height-integrated Joule heating rate

$$Q_J = \int_{z_1}^{z_2} \sigma_P(z) \left(\mathbf{E}_\perp + \mathbf{u}(z) \times \mathbf{B}(z)\right)^2 \mathrm{d}z \qquad [\mathrm{Wm}^{-2}]. \tag{3}$$

The height-integrated Joule heating rate Q_J can be determined from satellite observations (e.g. Foster et al., 1983; Rich et al., 1991; Palmroth et al., 2005). To determine the vertical profile of the local Joule heating rate q_J, incoherent scatter radar (ISR) measurements can be applied (e.g. Vickrey et al., 1982; Thayer, 1998, 2000; Kavanagh et al., 2022). Global thermosphere-ionosphere models provide vertical profiles of q_J at all geographic locations and are therefore a valuable addition to local ISR measurements (e.g. Weimer, 2005; Deng & Ridley, 2007; Deng et al., 2009; Huang et al., 2012; Maute, 2017). However, it has been noted that ionosphere models tend to underestimate the actual Joule heating rate quite significantly (Codrescu et al., 1995; Deng & Ridley, 2007). The Thermosphere-Ionosphere-Electrodynamcis Global-Circulation-Model (TIE-GCM) (Richmond et al., 1992) therefore multiplies the Joule heating rate by a constant empirical factor of $f = 1.5$ (Codrescu et al., 1995; Emery et al., 1999). The aim of this study is to investigate the required scaling factor under various different conditions and whether a constant $f = 1.5$ is actually appropriate. We will compare Joule heating rates given by the TIE-GCM model with measurements from the EISCAT ISR.
An important point to consider is the representation of the polar plasma convection in ionosphere models. Since the plasma convection depends on the interaction of the IMF with the Earth's magnetic field, a physical convection model would require coupled modelling of the solar wind, the magnetosphere, and the ionosphere. However, ionosphere-thermosphere models generally apply empirical convection models. Two of the most commonly applied convection models are the *Heelis* model (Heelis et al., 1982) and the *Weimer* model (Weimer, 2005). The *Heelis* model applies the Kp index as input parameter which quantifies the geomagnetic activity from global magnetometer measurements. The *Weimer* model fits the electrostatic potential for given solar wind/IMF parameters using a set of spherical harmonics (Weimer, 2005). We use the Kan-Lee merging electric field E_{KL} (Kan & Lee, 1979) to combine the solar wind and IMF parameters applied by the *Weimer* convection model. It has been found that E_{KL} correlates well with the polar cap potential (Weimer, 1995). The Kan-Lee merging electric field is defined as

$$E_{KL} = v_{sw} B_T \sin^2\left(\frac{\theta}{2}\right) \tag{4}$$

with the solar wind velocity v_{sw}, $B_T = \left(B_y^2 + B_z^2\right)^{0.5}$, and $\theta = \arctan\left(B_y / B_z\right)$, with the interplanetary magnetic field components B_y and B_z in the GSM coordinate system (Laundal & Richmond, 2017). Since the TIE-GCM model can be driven by both the *Heelis* and the *Weimer* convection models, we will compare the performance of both models within TIE-GCM to obtain Joule heating rates for different forcing conditions.
It has been shown that the Joule heating rate strongly depends on the magnetic local time (MagLT) (Foster et al., 1983; Baloukidis et al., 2023) and therefore we will also investigate how the required f factor varies with MagLT.
Section 2 will introduce the EISCAT ISR instrument and the TIE-GCM model. The applied measurement mode as well as the geophysical conditions during the measurements will be described. In Sec. 3, we will show how local and height-integrated Joule heating rates are determined from both measurements and model results. This includes an

introduction to the *stochastic inversion* method that is applied to obtain 3D ion velocity and electric field vectors from ISR measurements. The comparison of measurement and model Joule heating rates and the required f factor is shown in Sec. 4 and the results are discussed in Sec. 5. Section 6 will conclude the paper and give an outlook on possible future investigations.

2 Measurements and models

2.1 EISCAT UHF incoherent scatter radar

The EISCAT Ultra High Frequency (UHF) ISR at Tromsø, Norway (69.6° N, 19.2° E) (Folkestad et al., 1983) has a peak transmission power of about $1.5 - 2$ MW. The radar transmission frequency is 930 MHz and the employed dish has a diameter of 32 m. This results in a beam width of about 0.7° corresponding to an antenna directive gain of approximately 48.1 dBi.

To obtain 3D electric field vectors, the EISCAT ISR can either be operated in combination with two remote receivers (tristatic) or in a beam-swing mode (monostatic) (Kavanagh et al., 2022). For this study, we will analyze approximately 2220 h of EISCAT measurements in the beam-swing mode, also known as *Common Programme (CP) 2*. In this mode, the radar dish is rotated through four measurement positions with a total cycle time of 6 min, and the beam-aligned ion velocity is measured in each position. The time resolution of ~ 0.1 h results in approximately 22,200 measurement points. The EISCAT *CP 2* and other experiment modes are described in Tjulin (2021).

Following Nygrén et al. (2011), we perform a *stochastic inversion* to obtain the F-region 3D ion velocity vector. The ionospheric electric field can be calculated from the ion velocities. The method and its application in this study are described in more detail in Sec. 3. Other parameters available from the ISR measurements are the electron density N_e, and the ion/electron temperatures T_i and T_e. In the E-region, these parameters are binned in 13 altitude gates with a vertical resolution of 5 km at 95−125 km and 10 km at 135−185 km altitude.

As mentioned before, we will investigate Joule heating rates for different geophysical conditions (Kp index and E_{KL}) and magnetic local times. Table 1 gives the distribution of measurement time with Kp index and E_{KL}.

Kp	**measurement time [h]**	**E_{KL}** [$\mathrm{mVm^{-1}}$]	**measurement time [h]**
0	186.6	**$0 - 0.1$**	484.2
0.333	311	**$0.1 - 0.2$**	328.2
0.667	263.5	**$0.2 - 0.35$**	410.8
1	195.7	**$0.35 - 0.5$**	360.9
1.333	160.3	**$0.5 - 0.7$**	245.1
1.667	182.5	**$0.7 - 0.9$**	130.9
2	156.1	**$0.9 - 1.15$**	120.7
2.333 - 2.667	206.7	**$1.15 - 1.6$**	81.5
3 - 3.333	168	**> 1.6**	60.5
3.667 - 4	125		
4.333 - 5	139		
5.333 - 6	62.1		
> 6	35.6		
$\sum$	**2192.1**	$\sum$	**2222.8**

Table 1. Distribution of measurement time with Kp index and E_{KL}.

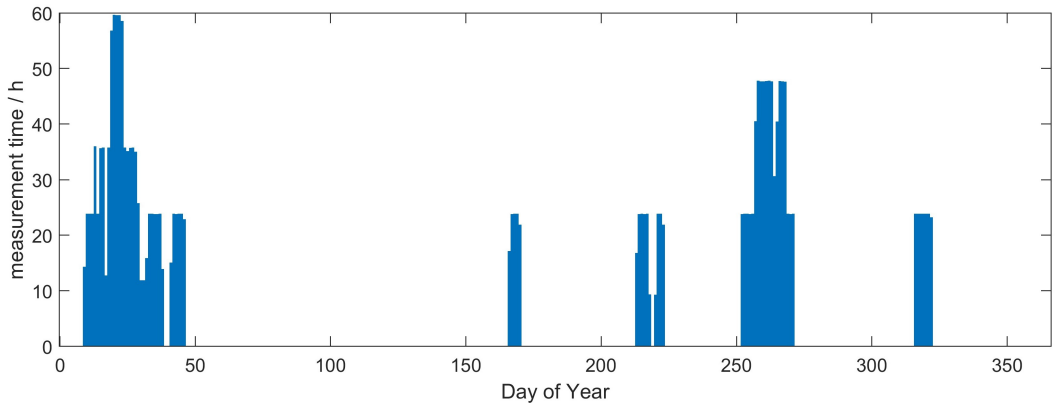

Figure 1. Seasonal distribution EISCAT measurement time included in the database

Investigating the bins given in Tab. 1 is only possible if the values are taken throughout the entire day and MagLT variations are neglected. Tables 2 and 3 give the bin resolution and measurement time per bin if variations with Kp index/E_{KL} and MagLT are investigated simultaneously.

Kp/MagLT	**03 - 09**	**09 - 15**	**15 - 21**	**21 - 03**	$\sum$
0 - 2	312	380.7	406.7	356.3	**1455.7**
2 - 4	128.3	136.7	137.4	97.3	**499.7**
4 - 9	51.3	45.2	66.5	73.7	**236.7**
$\sum$	**491.6**	**562.6**	**610.6**	**527.3**	**2192.1**

Table 2. Distribution of measurement time in hours with respect to Kp index and MagLT.

E_{KL} [mVm^{-1}] /MagLT	**03 - 09**	**09 - 15**	**15 - 21**	**21 - 03**	$\sum$
$0 - 0.2$	164	213.5	215	219.9	**812.4**
$0.2 - 0.5$	183.5	225.4	181.1	181.7	**771.7**
> 0.5	149	135.8	218.5	135.4	**638.7**
$\sum$	**496.5**	**574.7**	**614.6**	**537**	**2222.8**

Table 3. Distribution of measurement time in hours with respect to E_{KL} and MagLT.

A seasonal dependence of the Joule heating rate and the required scaling factor has been shown before (Foster et al., 1983; Emery et al., 1999). Figure 1 shows the distribution of the EISCAT measurements by day of year. It can be seen that most EISCAT CP2 measurements took place in January or around the September equinox. The distribution shown in Fig. 1 does not allow to investigate the seasonal dependence of the Joule heating rates and the required scaling. For the results shown in this paper, all measurements have been considered independent of the day of year.

2.2 TIE-GCM

The Thermosphere-Ionosphere-Electrodynamic General-Circulation-Model (TIE-GCM) (Richmond et al., 1992) is a global model of the coupled ionosphere-thermosphere system. The lower boundary is at about 96 km altitude where atmospheric dynamics are driven by the climatologies of several atmosphere models. The TIE-GCM output is given on a $2.5^\circ \times 2.5^\circ$ longitude-latitude grid with a time resolution of 1h. The vertical resolution is 1/4 in scale height units equivalent to a resolution of $\sim 2-18$ km. The data presented in this paper was generated from several runs performed with the TIE-GCM Model Version 2.0.
As mentioned in Sec. 1, the polar plasma potential, and hence the electric field, is given by an empirical convection model. Both the *Heelis* model (Heelis et al., 1982) and the *Weimer* model (Weimer, 2005) can be applied for that purpose. We performed two TIE-GCM runs for each EISCAT measurement, driven with either of the two convection models. The model data is binned into the same E-region altitude gates as the EISCAT plasma parameters. Since the model time resolution is lower than the measurement time resolution, we apply a nearest-neighbor extrapolation on the model data.

3 Method

The application of *stochastic inversion* to infer 3D ion velocity vectors from EISCAT beam-swing measurements is described in detail by Nygrén et al. (2011). We will summarize the implementation of the method for this paper and refer to Nygrén et al. (2011) for further information. The *stochastic inversion* method allows solving the linear problem

$$\mathbf{M} = \mathbf{A} \cdot \mathbf{x} + \epsilon \tag{5}$$

where the vector of unknown variables $\mathbf{x}$ is determined from the measurement vector $\mathbf{M}$ under consideration of the measurement uncertainties ϵ. This requires an adequate formulation of the theory matrix $\mathbf{A}$.
In the F-region ionosphere, the east- and northward ion velocities v_E^F and v_N^F can be assumed constant with altitude while the vertical ion velocity v_z^F changes with height (Nygrén et al., 2011). Therefore, the unknown vector $\mathbf{x}$ for each 6 min beam-swing cycle consists of one v_E^F value, one v_N^F values, and n_G $v_z^{F_G}$ values where n_G is the number of pre-defined F-region altitude gates. We define $n_G = 14$ altitude gates ranging from $230 - 515$ km altitude with a resolution of 15 km ($230-260$ km), 20 km ($280-360$ km), and 25 km ($390-515$ km). Ideally, one measurement cycle consists of four pointing directions and therefore the total number of beam-aligned ion velocity measurements for each beam-swing cycle is $4{\cdot}n_G$. It has to be considered that the fit of the incoherent scatter spectrum does not converge for one or more beams during some cycles but for the further explanation we will assume the ideal case of four measurements per cycle. For each measurement position, the azimuth angle α and the elevation angle β are known and the measurements can be expressed by the standard radial wind equation

$$M_i^G = \sin\alpha_i \cos\beta_i v_E^F + \cos\alpha_i \cos\beta_i v_N^F + \sin\beta_i v_z^{F_G} \tag{6}$$

for $i = [1, 4]$. The transformation coefficients in Eq. 6 give the ith line of the theory matrix $\mathbf{A}_G$ for a single altitude gate. Repeating this for each altitude gate gives the complete theory matrix $\mathbf{A}$ (see Nygrén et al., 2011, Eq. 21).
Since the F-region ionosphere can be assumed to be collisionless, the perpendicular electric field can be approximated by the electric drift formula

$$\mathbf{E}_\perp = -\mathbf{v}^F \times \mathbf{B}. \tag{7}$$

As magnetic field B, the International Geomagnetic Reference Field (IGRF) (Barraclough, 1988; Alken et al., 2021) is employed. $\mathbf{E}_\perp$ is calculated at 300 km altitude and linearly scaled with the increasing magnetic field strength at lower altitudes. $\mathbf{E}_\perp$ can then be applied to calculate the local Joule heating rate in the E-region given by Eq. 2. Numerical integration of the 13 E-region altitude gates gives the height-integrated Joule heating rate Q_J. Although the TIE-GCM model gives the local Joule heating rate q_J as an output variable, we calculate it from Eq. 2 assuming the F-region $\mathbf{v}^F$ at 300 km altitude. The equivalent calculation of measurement and model Joule heating rates assures that any deviations are caused by the differences in plasma convection.
The Pedersen conductivity in Eq. 2 is given as (Baumjohann & Treumann, 1996)

$$\sigma_P = \left(\frac{\nu_{en}}{\nu_{en}^2 + \Omega_e^2} + \frac{m_e}{m_i} \frac{\nu_{in}}{\nu_{in}^2 + \Omega_i^2} \right) \frac{N_e e^2}{m_e}. \tag{8}$$

The ion/electron-neutral collision frequencies ν_{in} and ν_{en}, ion/electron gyro-frequencies Ω_i and Ω_e and the mean ion mass m_i are taken from the TIE-GCM model runs for both the measurement and the model calculation. The electron density N_e is taken from EISCAT measurements when calculating the observed Joule heating rates and from the TIE-GCM output when calculating the modeled Joule heating rates.
The vertical profile of the neutral wind $\mathbf{u}(z)$ in Eq. 2 and 3 is taken from the TIE-GCM model and assumed for the calculation of both the measurement and the model Joule heating rates. Especially for periods of low geomagnetic activity, the neutral wind contribution to the Joule heating rate can not be neglected (Vickrey et al., 1982; Baloukidis et al., 2023).

4 Results

After calculating the vertical Joule heating profiles from measurement and model data for each time-point, the profiles are binned with respect to the Kp index, E_{KL}, and MagLT. For each bin, a median measurement profile $q_J^E(z)$ and two median model profiles $q_J^M(z)$, one for *Heelis*- and one for *Weimer*-driven model runs, are calculated. The optimum empirical scaling factor f is determined by a non-linear least-square fit of $q_J^E(z) - f \cdot q_J^M(z) = 0$. This is demonstrated in Figure 2 for 230 h of data during September 2005 with $Kp > 2$ conditions.

The model profiles in Fig. 2 a) are linearly scaled to fit the measurement q_J profile which results in the profiles shown in Fig. 2 b). From the non-linear least-square fit, it is found that the optimum scaling factors for the model runs with *Heelis* and *Weimer* plasma convection are $f_H = 1.60$ and $f_W = 1.41$. These are very close to the default value $f = 1.5$ in the TIE-GCM model.
For further analysis, an extended database of approximately 2220 h of EISCAT measurements and TIE-GCM simulations is applied. The data is binned according to the Kp index and E_{KL} ranges given in Tab. 1. We investigate the optimum profile scaling factor f and the mean-squared difference of the vertical Joule heating rate profiles. The mean-squared difference is calculated as $MSD = 1/n_z \cdot \sum_{n_z} \left(q_{n_z}^E - q_{n_z}^M \right)^2$ where $n_z = 13$ is the number of altitude gates, and q^E and q^M are the local Joule heating rates given by EISCAT measurements and model runs respectively. We also investigate the absolute and relative difference between measurement and model height-integrated Joule heating rates. Figure 3 shows the variation of these quantities with the Kp index.

For the TIE-GCM runs driven with the *Heelis* convection model, it can be seen in Fig. 3 a) that the model would require a significantly larger scaling factor to fit the EISCAT measurements at $Kp < 4$ conditions. In Fig. 3 b), c), and d), the results are shown for the application of the default $f = 1.5$ and the optimized f from Fig. 3 a). An adjustment of the scaling factor reduces the MSD in Fig. 3 b) by two orders of magnitude.

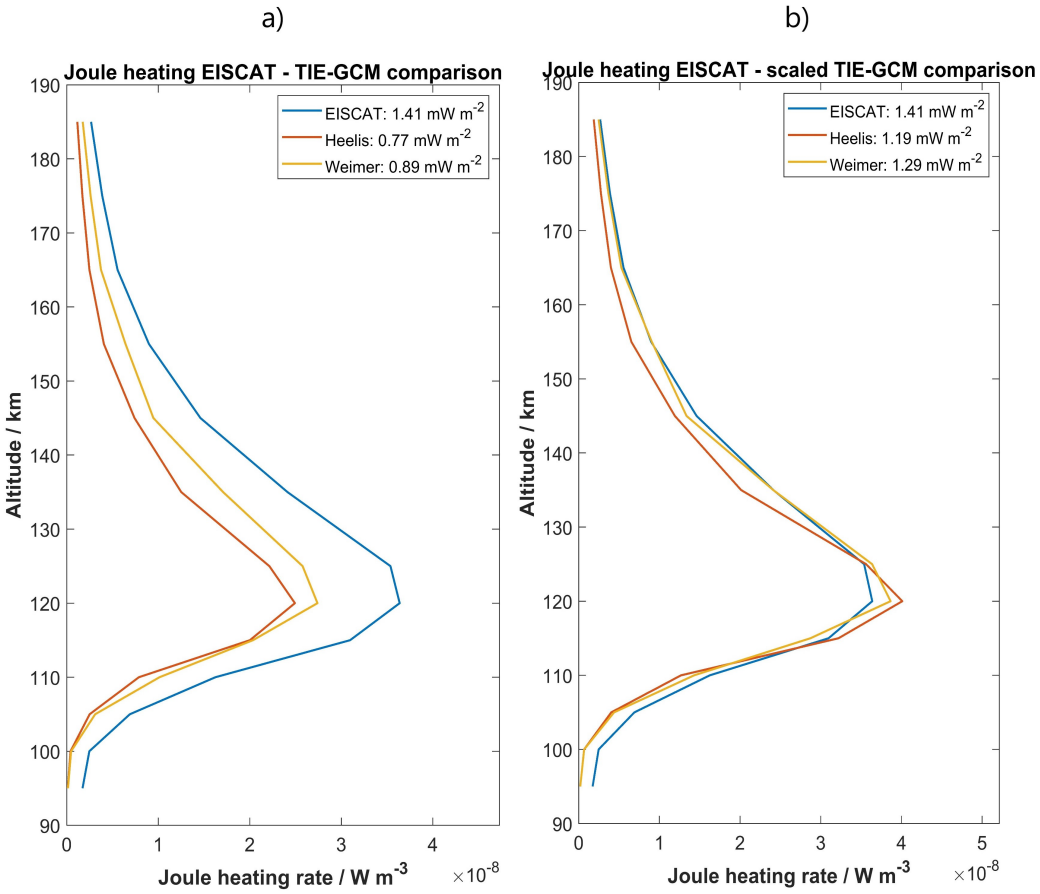

Figure 2. a) Joule heating profiles from EISCAT measurements and TIE-GCM simulations with both *Heelis* and *Weimer* plasma convection for $Kp > 2$. b) The two model profiles are scaled with the optimum scaling factors $f_H = 1.60$ and $f_W = 1.41$ to fit the measurement profile.

Due to the generally lower Joule heating rates at $Kp < 4$, the absolute difference $\Delta Q_{abs} = Q_J^E - Q_J^M$ in Fig. 3 c) is very low. Nevertheless, it can be seen that the height-integrated Joule heating rate gets slightly closer to the measurement results by adjusting the scaling factor for *Heelis*-driven runs at $Kp < 4$. The relative difference $\Delta Q_{rel} = \left(Q_J^E - Q_J^M\right)/Q_J^E$ in Fig. 3 d) would be notably reduced. For $Kp > 4$, the default scaling factor $f = 1.5$ seems to be appropriate or even too large for *Heelis*-driven TIE-GCM runs. The MSD of the Joule heating rate profiles is significantly larger at $Kp > 4$ than at lower geomagnetic activity and could be decreased by adjusting the scaling factor. However, ΔQ_{abs} and ΔQ_{rel} are actually increased for the adjusted scaling factor at $Kp \sim 5$. At $Kp > 5$, on the other hand, the height-integrated Joule heating rate is far too high for the default $f = 1.5$ and adjusting the scaling factor would bring it significantly closer to the measurement results.

The TIE-GCM runs driven with the *Weimer* convection model require a scaling factor $f > 1.5$ at $Kp < 4$ conditions. The MSD of measurement and model Joule heating rate profiles would be significantly reduced by adjusting the scaling factor. However, the measurement-to-model difference of the height-integrated Joule heating rate is not notably lower than for $f = 1.5$. The relative difference would generally be reduced at $Kp < 4$ by adjusting the scaling factor. At $Kp > 5$, *Weimer*-driven model runs clearly underestimate the Joule heating rate. An adjustment of the scaling factor would signifi-

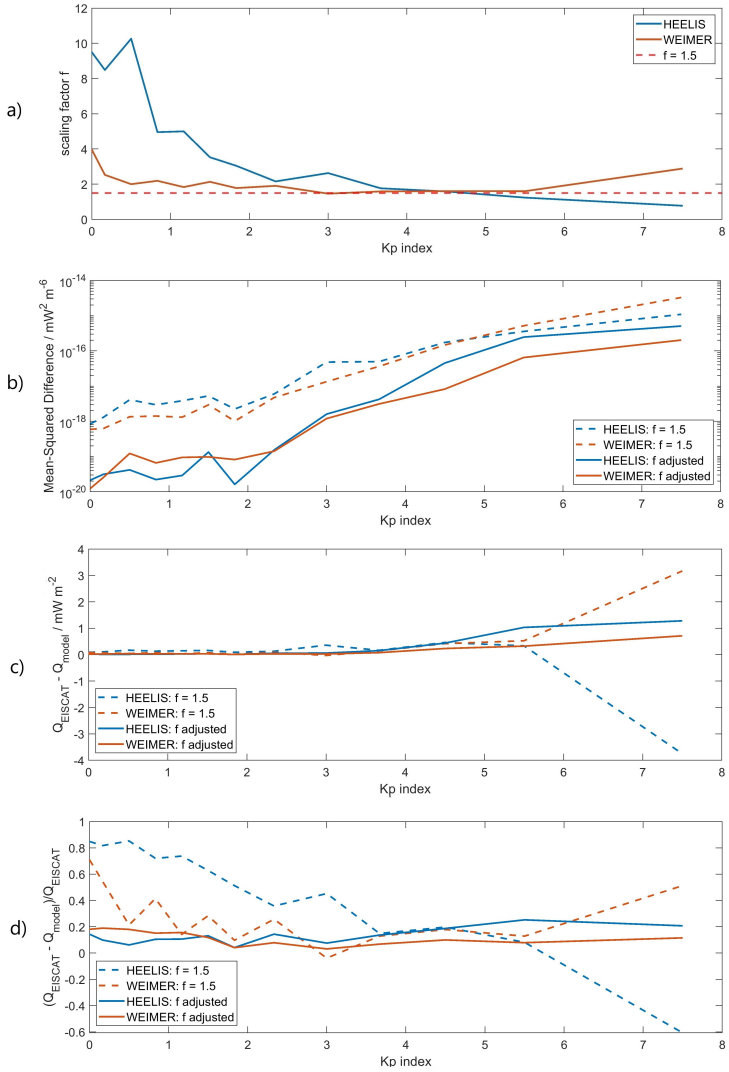

Figure 3. a) Scaling factor f, b) the mean-squared difference of the median measurement and model profiles, c) the absolute and d) the relative difference of measurement and model height-integrated Joule heating rates. The dotted lines in b), c), and d) give the results in case the scaling factors from a) are applied to the model runs.

cantly reduce the profile MSD as well as ΔQ_{abs} and ΔQ_{rel} of measurement and model height-integrated Joule heating rates.

In summary, the TIE-GCM model results show very different behaviour for *Heelis*- and *Weimer*-driven polar plasma convection. For the default scaling factor $f = 1.5$, the *Heelis*-driven model runs underestimate the Joule heating rate at $Kp < 4$ and overestimate it at $Kp > 5$. An adjustment of the scaling factor might significantly reduce the difference between measurement and model results. For *Weimer*-driven model runs, the default $f = 1.5$ seems to work considerably well at $Kp < 4$. While the MSD of the Joule heating rate profiles could be slightly decreased by adjusting the scaling factor, the height-integrated Joule heating rate would remain approximately the same. At $Kp > 4$, however, the Joule heating rates are clearly underestimated for the $f = 1.5$ case and an adjustment of the scaling factor would reduce the gap between EISCAT measurements and model results.

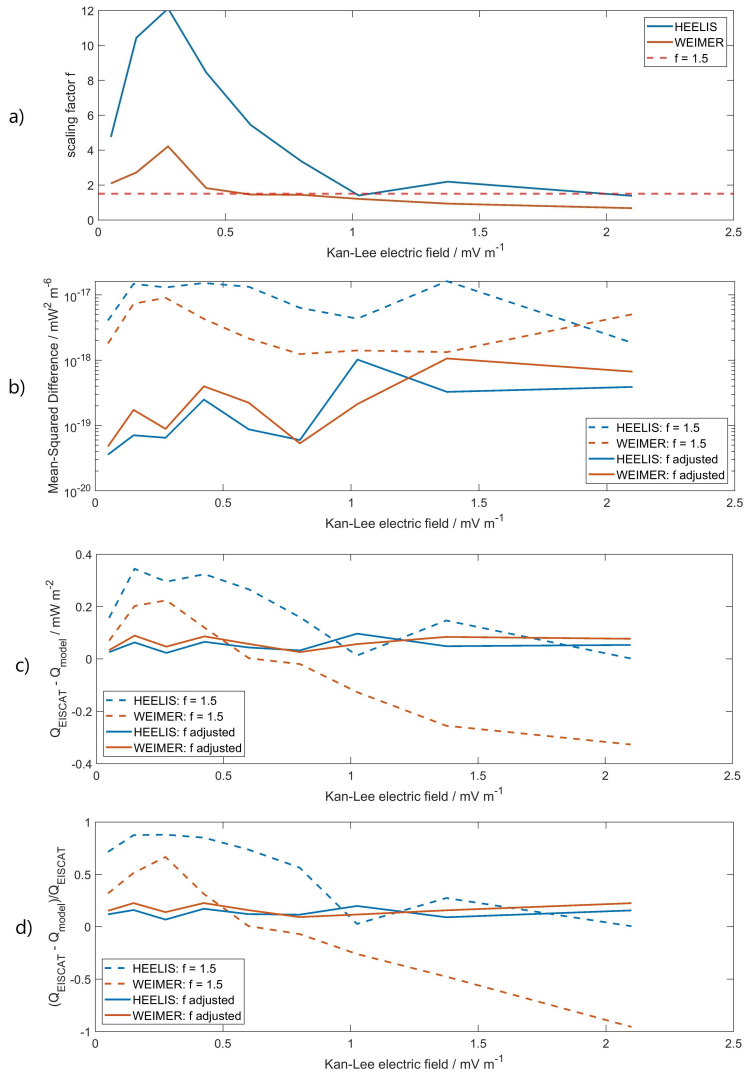

Figure 4. a) Scaling factor f, b) the mean-squared difference of the median measurement and model profiles, c) the absolute and d) the relative difference of measurement and model height-integrated Joule heating rates. The dotted lines in b), c), and d) give the results in case the scaling factors from a) are applied to the model runs.

As mentioned in Sec. 1, the *Weimer* convection model determines the polar plasma potential from solar wind and IMF parameters. Therefore, the analysis above is repeated for the Kan-Lee merging electric field E_{KL} bins listed in Tab. 1. The results are shown in Fig. 4.

The required scaling factor in Fig. 4 a) shows that *Heelis*-driven TIE-GCM runs generally underestimate the Joule heating rate for most E_{KL} values. An adjustment of the scaling factor would reduce the MSD of the vertical Joule heating rate profiles by at least one order of magnitude for all E_{KL} values as shown in Fig. 4 b). This can also be seen in Fig. 4 c), where the absolute measurement-to-model difference of height-integrated Joule heating rate would be decreased by adjusting the scaling factor at all conditions with the exception of $E_{KL} \sim 1$ mVm^{-1} and $E_{KL} \gtrsim 2$ mVm^{-1}. The same result is found for the relative difference in Fig. 4 d).

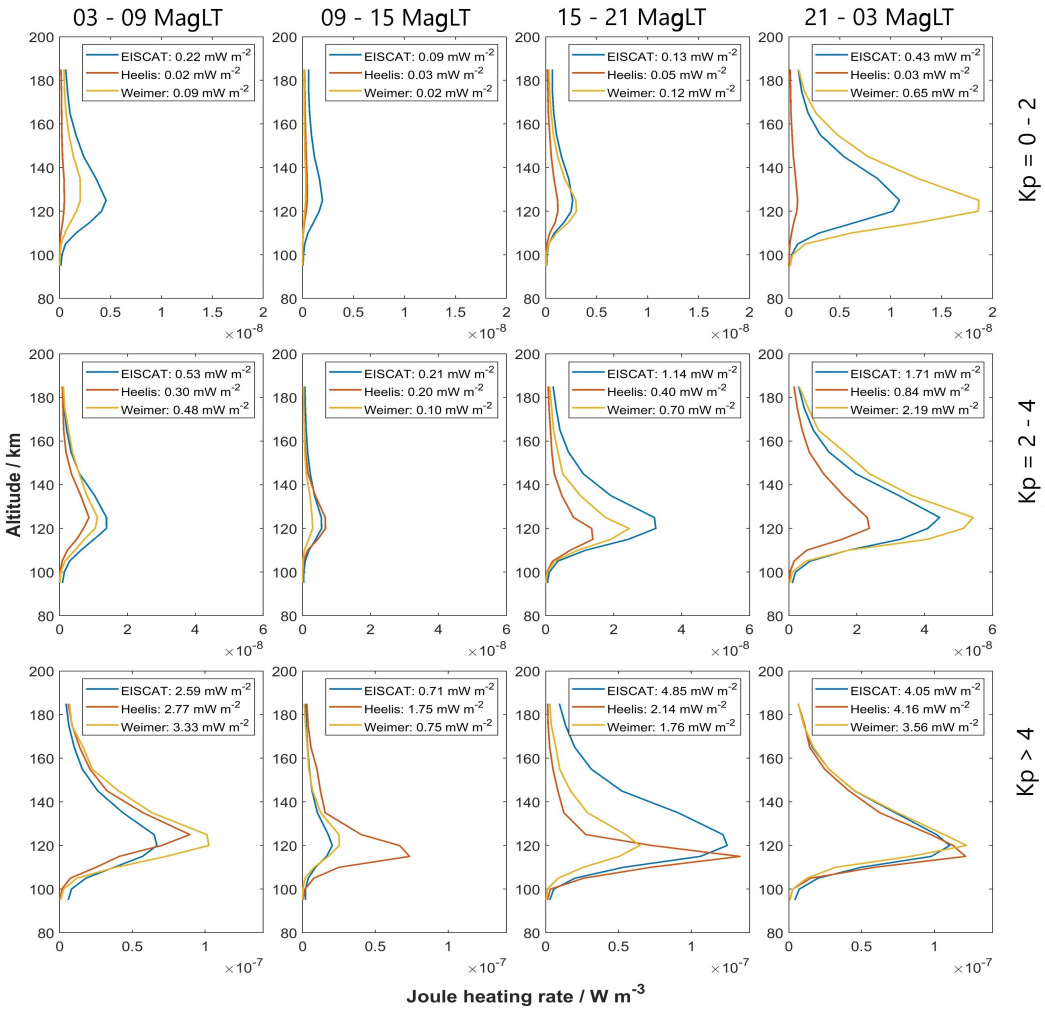

Figure 5. Vertical profiles of the Joule heating rate for 12 bins of varying Kp index and magnetic local time. The default $f = 1.5$ has been applied to the model Joule heating rate profiles. The respective height-integrated Joule heating rates are given in the legends.

For the *Weimer*-driven model runs, it is found in Fig. 4 a) that by applying a constant $f = 1.5$, the Joule heating rate is underestimated for $E_{KL} \lesssim 0.5$ mVm^{-1} and overestimated for $E_{KL} \gtrsim 1$ mVm^{-1}. Figure 4 c) and d) show that an adjustment of the scaling factor would reduce ΔQ_{abs} and ΔQ_{rel} of measurements and model runs for these E_{KL} ranges. Especially at $E_{KL} \gtrsim 1$ mVm^{-1}, the *Weimer*-driven model Joule heating rates would be significantly closer to the measurements if the scaling factor is adjusted.

It has been reported previously that the Joule heating rate varies strongly with the magnetic local time (Foster et al., 1983; Baloukidis et al., 2023). We will therefore investigate the Joule heating rates separately for four MagLT bins covering the dawn sector (03-09 MagLT), the noon sector (09-15 MagLT), the dusk sector (15-21 MagLT), and the midnight sector (21-03 MagLT). To obtain enough measurement time in each investigated bin, the Kp index and E_{KL} bins are enlarged as stated in Tab. 2 and 3. In total, we obtain vertical Joule heating rate profiles and the associated height-integrated Joule heating rates for 12 bins. Figure 5 shows the q_J profiles binned with respect to the Kp index and MagLT.

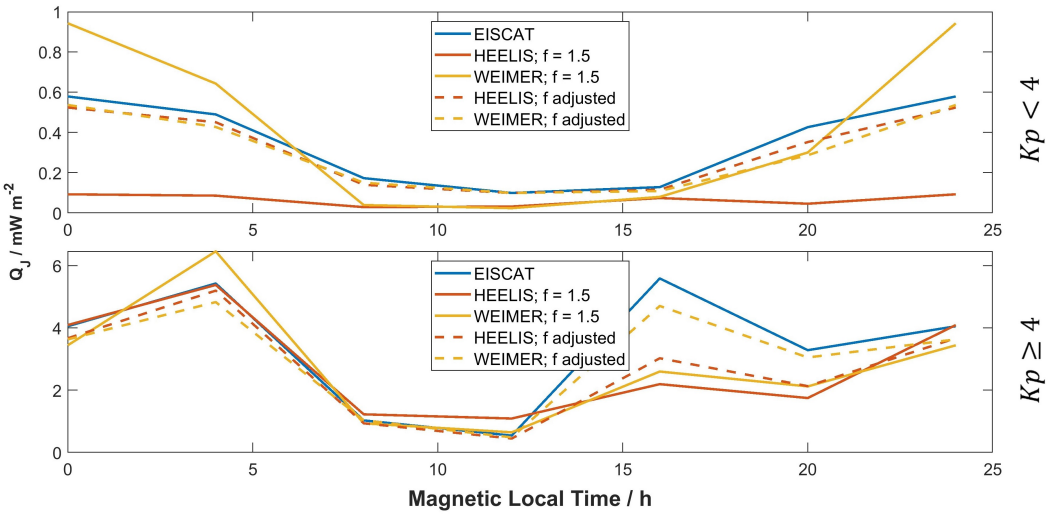

Figure 6. Variation of the height-integrated Joule heating rate Q_J with magnetic local time for $Kp < 4$ (top) and $Kp \geq 4$ (bottom). The model results are shown as dashed lines for the default $f = 1.5$ and solid lines for an adjusted scaling factor.

As expected, the Joule heating rate increases with the Kp index which can be seen from the maxima of the vertical profiles and the height-integrated Joule heating rates given in Fig. 5. This is found for both measurement and model Joule heating rates. The measurements show that the Joule heating rate is generally lowest in the noon MagLT sector and largest in the midnight MagLT sector. The important exception is for $Kp > 4$, where the largest measurement Joule heating rates are actually found in the dusk MagLT sector. For the model runs, both driven by *Heelis* and *Weimer* convection, it is found that the Joule heating rate is lowest in the noon sector and largest in the midnight sector for all Kp ranges. The model profiles shown in Fig. 5 have been scaled with the default factor $f = 1.5$. The *Heelis*-driven model runs give generally lower Joule heating rates than the EISCAT measurements for $Kp < 4$. This agrees with Fig. 3 where it has been shown that *Heelis*-driven runs require a larger than default scaling factor at $Kp < 4$. At $Kp > 4$, however, the Joule heating rates approximately fit the EISCAT measurements or even exceed them for the noon sector, where EISCAT measured the overall lowest Joule heating rates.
At $Kp < 4$, the default-scaled *Weimer*-driven TIE-GCM runs show slightly lower Joule heating rates than the measurements at all magnetic local times except for the midnight MagLT sector. For $Kp > 4$, however, the q_J profiles from *Weimer*-driven runs fit the measurement profiles very well, except for the dusk MagLT sector. Here, the Joule heating is clearly underestimated by the model runs.
In summary, it can be seen from Fig. 5 that the magnetic local time very much impacts the vertical Joule heating profile and how well the model runs fit the measurements. This can also be seen from the variation of the height-integrated Joule heating rate with magnetic local time shown in Fig. 6. Two cases of geomagnetic activity, $Kp < 4$ and $Kp \geq 4$, are distinguished.

As noticed before, Fig. 6 shows that Joule heating rates are largest during nighttime for $Kp < 4$. While the *Heelis*-driven runs give a very low height-integrated Joule heating rates at all MagLTs, Q_J from *Weimer*-driven runs is lower than the measurements during daytime and larger during nighttime. Adjusting the scaling factor would reduce the difference between EISCAT and model height-integrated Joule heating rates at all magnetic local times.

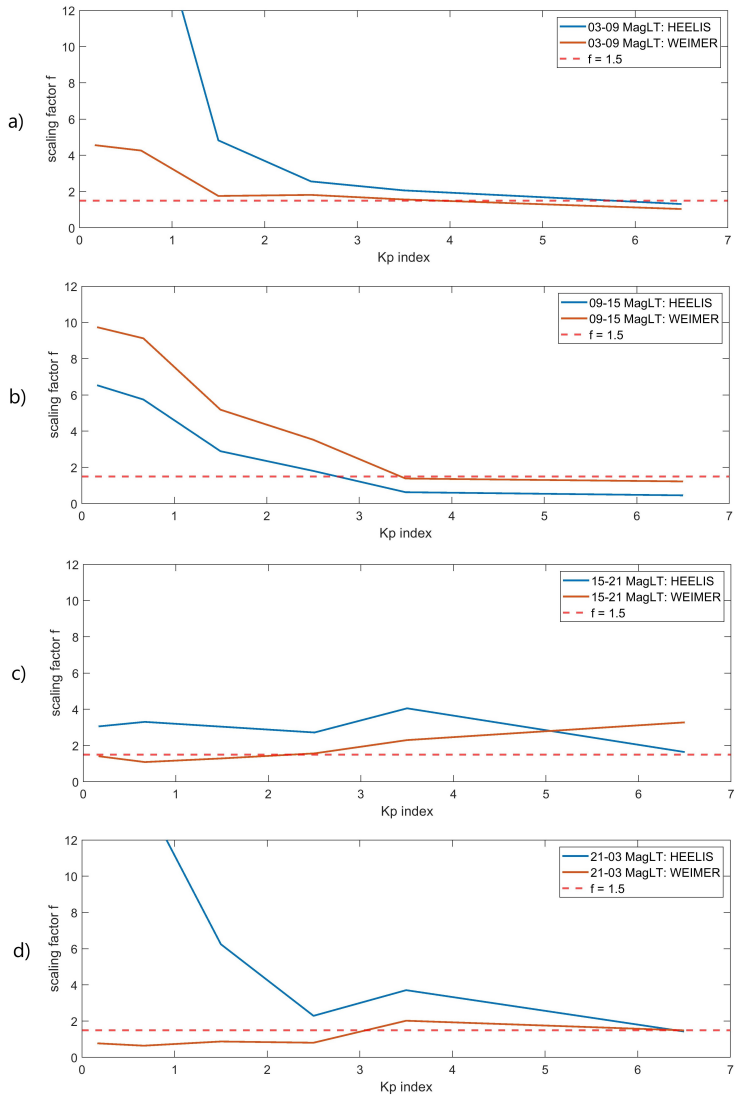

Figure 7. Kp index dependence of the required Joule heating scaling factor f for the different magnetic local time sectors a) 03-09, b) 09-15, c) 15-21, and d) 21-03.

At $Kp > 4$, the measured Q_J maximum is around 16 MagLT and the largest model Q_J are found around 4 MagLT. It can be seen in Fig. 5 that all model runs give distinctly larger Joule heating rates than the measurements for $Kp > 4$, 3 - 9 MagLT. It should be noted that at $Kp > 4$, the *Heelis*-driven runs scaled with $f = 1.5$ reproduce the measurement Q_J extremely well at about 0 - 6 MagLT, while the *Weimer*-driven runs give Q_J very close to the measurements at around 6 - 12 MagLT. Therefore, the required scaling factor does not only change with Kp index and convection model but also with magnetic local time. Similar to Fig. 3 a), the required scaling factors for the dawn, noon, dusk, and midnight MagLT sectors are shown in Fig. 7.

The large scaling factor required for *Heelis*-driven runs at low Kp values seen in Fig. 3 is mostly caused by the dawn and midnight sectors (see Fig. 7 a and d). During the noon and dusk sector in Fig. 7 b) and c), the *Heelis*-driven runs only slightly underestimate the Joule heating for low Kp values. At high Kp values, the differences be-

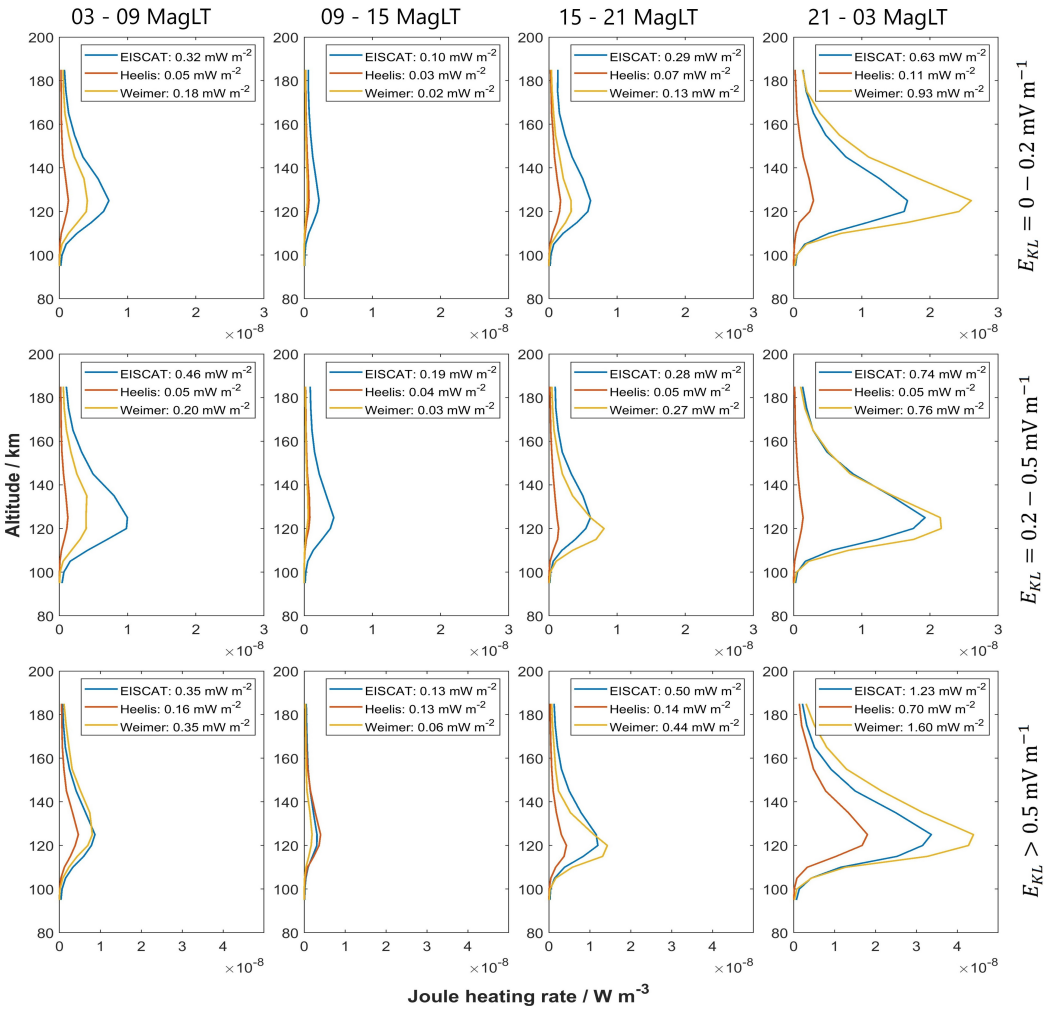

Figure 8. Vertical profiles of the Joule heating rate for 12 bins of varying E_{KL} and magnetic local time. The default $f = 1.5$ has been applied to the model Joule heating rate profiles. The respective height-integrated Joule heating rates are given in the legends.

tween the measurement and model Joule heating rates seems to be well accounted for by the default $f = 1.5$ except for the noon sector where f should be reduced.
The *Weimer*-driven TIE-GCM runs seem to underestimate the Joule heating rate at low Kp values during the dawn and noon sectors. During the dusk and midnight sectors, $f = 1.5$ seems to cover the measurement-model difference well or even overestimate it. In Fig. 3, it has been noted that *Weimer*-driven model runs tend to underestimate the Joule heating rate more than covered by $f = 1.5$ for $Kp > 4$. As it can be seen in Fig. 7 c), this is actually only the case for the dusk MagLT sector where EISCAT measurements showed the largest Joule heating rates. During all other MagLT sectors, $f = 1.5$ appears to be very close to the required scaling factor at $Kp > 4$.
In summary, the required scaling factor changes significantly not only with the Kp index but also with the magnetic local time. Adjusting the scaling factor f with respect to MagLT might therefore result in a notably better agreement of measurement and model results. The E_{KL} dependence for different MagLT sectors is investigated with the bins listed in Tab. 3. The Joule heating profiles for the respective bins are shown in Fig. 8, the model run profiles have again been scaled with $f = 1.5$.

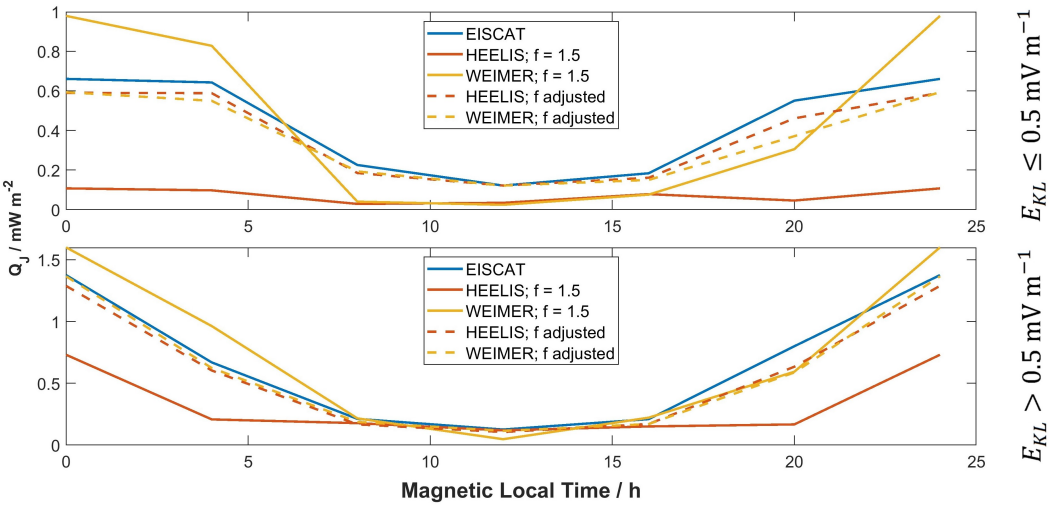

Figure 9. Variation of the height-integrated Joule heating rate Q_J with magnetic local time for $E_{KL} < 0.5$ mVm^{-1} (top) and $E_{KL} \geq 0.5$ mVm^{-1} (bottom). The model results are shown as dashed lines for the default $f = 1.5$ and solid lines for an adjusted scaling factor.

It can be seen that the Joule heating rate generally but not strictly increases with E_{KL}. Measurements and model runs both give the strongest Joule heating for the midnight MagLT sector and the weakest Joule heating for the noon MagLT sector at all E_{KL} conditions. The MagLT dependence of the Joule heating rate therefore agrees well with Fig. 5.
The *Heelis*-driven TIE-GCM runs give too low Joule heating rates in all 12 bins, indicating that in these runs E_{KL} and the Joule heating rate are not well correlated. This can be explained by the fact that *Heelis*-driven runs do not apply any solar wind information as input. However, the *Weimer*-driven runs show a behavior very similar to what has been found in Fig. 5. At $E_{KL} > 0.5$ mVm^{-1} and in the MagLT midnight sector, *Weimer*-driven TIE-GCM runs give Joule heating profiles that fit the measurement profiles very well or even exceed them. At all other conditions, the model runs tend to underestimate the Joule heating. Figure 9 displays the variation of the height-integrated Joule heating rate with MagLT, distinguished for the two cases $E_{KL} < 0.5$ mVm^{-1} and $E_{KL} \geq 0.5$ mVm^{-1}.

For $E_{KL} < 0.5$ mVm^{-1}, the results are nearly equivalent to the $Kp < 4$ case shown in Fig. 6. Q_J is generally largest at MagLT midnight and *Heelis*-driven runs give extremely low Joule heating rates at all magnetic local time sectors. The *Weimer*-driven runs overestimate the heating rate at nighttime and underestimate it at daytime. Adjusting the scaling factor would significantly decrease the difference between measurement and model Q_J for all magnetic local times.
For $E_{KL} \geq 0.5$ mVm^{-1}, the results are quite similar to the low geophysical activity conditions. The height-integrated Joule heating rate is largest in measurements and models during the midnight MagLT sector. The *Heelis*-driven TIE-GCM runs reproduce the measurement Q_J well at about 8 - 16 MagLT but strongly underestimate the Joule heating for all other times. This suggests that the Kan-Lee merging electric field E_{KL} does not have much impact on the Joule heating during magnetic local daytime. The *Weimer*-driven runs also reproduce the measurement results very well at about 8 - 16 MagLT and slightly overestimate Q_J at most other magnetic local times. An adjustment of the scaling factor would improve the height-integrated Joule heating rate in both *Heelis*- and *Weimer*-driven runs at all magnetic local times compared to the EISCAT measurements.

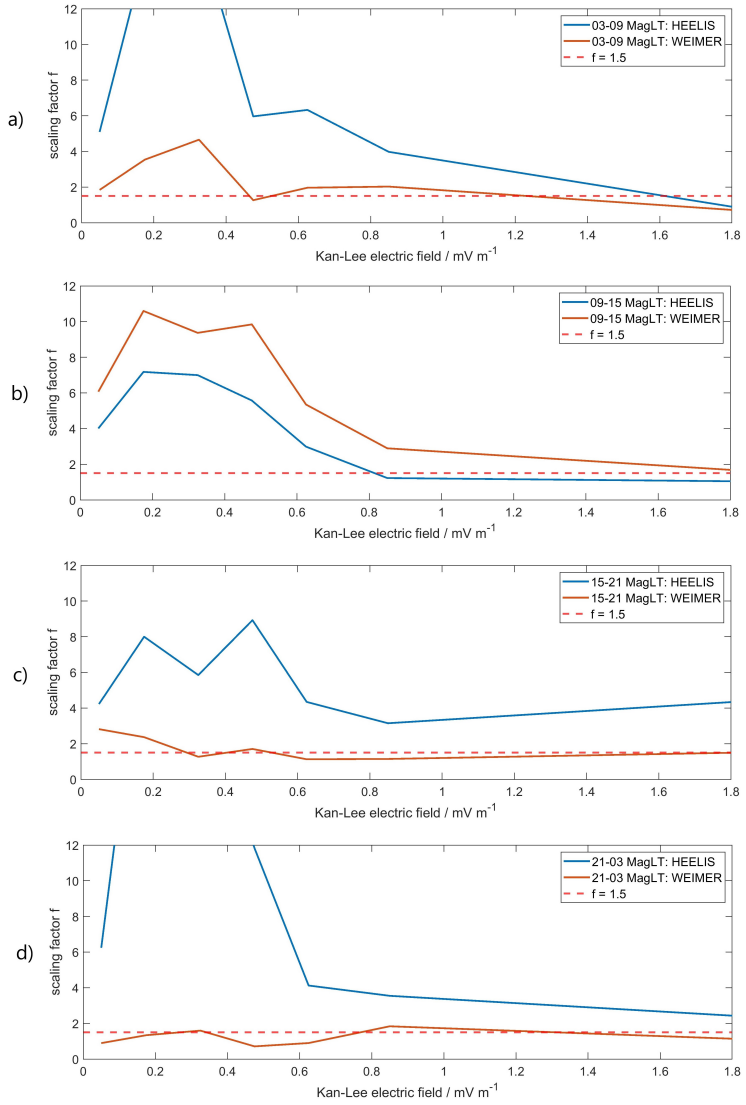

Figure 10. E_{KL} dependence of the required Joule heating scaling factor f for the different magnetic local time sectors a) 03-09, b) 09-15, c) 15-21, and d) 21-03.

For the four MagLT sectors investigated in Fig. 8, the required scaling factors at different E_{KL} conditions are shown in Fig. 10.

The distinctly larger Joule heating scaling required for *Heelis*-driven model runs at low E_{KL} values is mostly rooted in the dawn and midnight MagLT sectors shown in 10 a) and d). This is similar to what has been found in Fig. 7. However, as has been noted in Fig. 8, the default $f = 1.5$ is too low for *Heelis*-driven runs under most E_{KL} and MagLT conditions. The exception is for $E_{KL} \gtrsim 0.8$ mVm^{-1} during the MagLT noon sector in Fig. 10 where a scaling factor slightly lower than $f = 1.5$ would lead to the best fit of measurement and model. This is equivalent to what has been found for $Kp > 3$ in Fig. 7.

For the *Weimer*-driven runs, the required scaling factor is very close to the default $f = 1.5$ for the majority of E_{KL} conditions and magnetic local times. The clearest deviation is found for $E_{KL} \lesssim 0.6$ mVm^{-1} during the noon MagLT sector though the required scaling factor is larger than 1.5 for all E_{KL} conditions in that sector. This agrees very well

with Fig. 6, 7 b), and 9 which all showed that the Joule heating rate is underestimated around MagLT noon time in *Weimer*-driven TIE-GCM runs.
The optimum scaling factors f_H and f_W for *Heelis*- and *Weimer*-driven TIE-GCM runs for 13 Kp bins and 9 E_{KL} bins are shown in Tab. 4. Tables 5 and 6 give the optimum scaling factors f_H and f_W for the four investigated MagLT sectors in three bins of Kp index and E_{KL} respectively.

Kp	$\mathbf{f_H}$	$\mathbf{f_W}$	$\mathbf{E_{KL}}$ [$\mathrm{mVm^{-1}}$]	$\mathbf{f_H}$	$\mathbf{f_W}$
0	9.50	3.97	$\mathbf{0-0.1}$	4.76	2.09
0.333	8.49	2.53	$\mathbf{0.1-0.2}$	10.44	2.72
0.667	10.26	2.00	$\mathbf{0.2-0.35}$	12.11	4.21
1	4.96	2.19	$\mathbf{0.35-0.5}$	8.44	1.82
1.333	5.00	1.84	$\mathbf{0.5-0.7}$	5.44	1.45
1.667	3.53	2.14	$\mathbf{0.7-0.9}$	3.35	1.44
2	3.05	1.78	$\mathbf{0.9-1.15}$	1.40	1.21
2.333 - 2.667	2.16	1.91	$\mathbf{1.15-1.6}$	2.19	0.93
3 - 3.333	2.63	1.46	$\mathbf{>1.6}$	1.38	0.67
3.667 - 4	1.77	1.59			
4.333 - 5	1.59	1.61			
5.333 - 6	1.24	1.60			
$\mathbf{>6}$	0.77	2.89			

Table 4. Adjusted scaling factors f_H and f_W for *Heelis*- and *Weimer*-driven model runs with respect to Kp index and E_{KL}.

Kp/MagLT	**03 - 09**	**09 - 15**	**15 - 21**	**21 - 03**
0 - 2	$f_H = 13.32$ $f_W = 3.16$	$f_H = 5.59$ $f_W = 8.31$	$f_H = 3.45$ $f_W = 1.40$	$f_H = 18.91$ $f_W = 0.87$
2 - 4	$f_H = 2.68$ $f_W = 1.88$	$f_H = 1.32$ $f_W = 2.90$	$f_H = 3.57$ $f_W = 2.20$	$f_H = 2.89$ $f_W = 1.24$
4 - 9	$f_H = 1.31$ $f_W = 1.04$	$f_H = 0.46$ $f_W = 1.23$	$f_H = 1.64$ $f_W = 3.28$	$f_H = 1.43$ $f_W = 1.49$

Table 5. Adjusted scaling factor f_H and f_W for *Heelis*- and *Weimer*-driven model runs with respect to the Kp index and MagLT.

5 Discussion

Codrescu et al. (1995) showed that a scaling of the Joule heating in global circulation models is necessary to account for the contribution of processes on time-scales not resolved in the models. The factor $f = 1.5$ has been implemented in the TIE-GCM model as the default factor and, as shown in this study, seems to be appropriate as average factor for all convection models, magnetic local times and geophysical conditions. The general trend that the largest q_J occurs around midnight and the lowest q_J is observed around noon magnetic local time agrees well with previous studies (e.g. Rodger et al., 2001; Baloukidis et al., 2023). The exception is that for EISCAT measurements at $Kp > 4$, the strongest Joule heating is found in the dusk MagLT sector. Foster et al. (1983) reported a maximum of Joule heating rates in the MagLT dusk sector for $3 \leq Kp \leq 6$ during summer. However, since our data includes comparably few measurements during summer,

$\mathbf{E_{KL}}$ [$\mathbf{mVm^{-1}}$] /MagLT	03 - 09	09 - 15	15 - 21	21 - 03
$\mathbf{0 - 0.2}$	$f_H = 8.90$ $f_W = 2.52$	$f_H = 4.49$ $f_W = 6.62$	$f_H = 5.61$ $f_W = 2.86$	$f_H = 9.27$ $f_W = 1.00$
$\mathbf{0.2 - 0.5}$	$f_H = 13.00$ $f_W = 3.42$	$f_H = 7.62$ $f_W = 10.63$	$f_H = 6.25$ $f_W = 1.18$	$f_H = 21.15$ $f_W = 1.27$
$\mathbf{> 0.5}$	$f_H = 3.04$ $f_W = 1.51$	$f_H = 1.28$ $f_W = 2.61$	$f_H = 4.47$ $f_W = 1.30$	$f_H = 2.92$ $f_W = 1.14$

Table 6. Adjusted scaling factor f_H and f_W for *Heelis*- and *Weimer*-driven model runs with respect to E_{KL} and MagLT.

the dusk maximum of Joule heating found in this paper might not be related to the findings by Foster et al. (1983). Baloukidis et al. (2023) showed that this trend is also found in TIE-GCM runs driven by the *Weimer* convection model. However, the variation of Joule heating with magnetic local time is not exactly reproduced by the model which introduces increased heating rates for MagLT noon time and lower heating rates during the rest of the day (Baloukidis et al., 2023). Similarly, they showed an increase of the Joule heating rate with increasing Kp index, though the trend is not equally strong in measurements and models. The findings of (Baloukidis et al., 2023) could be mostly confirmed in this paper and extended by also considering *Heelis*-driven TIE-GCM runs as well as variations with the Kan-Lee merging electric field E_{KL}.

Past studies have shown that it is advantageous to adjust the scaling factor with regard to certain parameters, e.g. in Emery et al. (1999) $f = 1.5$ was applied in the winter and $f = 2.5$ in the summer hemisphere. Foster et al. (1983) showed a strong seasonal dependence of the height-integrated Joule heating rate. It is likely that this variation, similar to the variation with geophysical activity and MagLT, is not exactly reproduced by the models. However, as shown in Fig. 1, the measurements investigated in this paper are not equally spread across the year and, thus, a detailed analysis of the scaling parameter for all seasons with similar statistics is not yet feasible from the available database.

It should be considered, that not only the models but also the measurements do not resolve all processes contributing to the variability of Joule heating. Codrescu et al. (1995) noted that there is a considerable variability on time-scales $\lesssim$ 5 min that leads to an underestimation of Joule heating rates. The measurement resolution of 6 min applied in this paper, therefore, does not include the contribution of fast-dynamic processes either. Brekke and Kamide (1996) showed that frictional heating terms related to the inertia of the ions lead to a heating contribution of oscillating electric fields. Fast-changing electric fields on a time-scale $\sim$ 1 s could increase the maximum of the Joule heating rate profile by about 10% (Brekke & Kamide, 1996). However, these time-scales are currently far below the resolution of both ISR measurements and ionosphere models. But it can be assumed that the required scaling of model Joule heating rates has to be further adjusted once measurements are able to resolve shorter time-scales.

One major assumption for the present study was the application of TIE-GCM neutral winds and ion-neutral collision frequencies for both measurement and model calculations. It is possible to calculate neutral winds from EISCAT CP2 measurements (Brekke et al., 1973; Nozawa et al., 2010; Günzkofer et al., 2022) but this, in turn, requires knowledge of the ion-neutral collision frequency. The ion-neutral collision frequency can be measured from dual-frequency EISCAT experiments (Grassmann, 1993; Nicolls et al., 2014) which is not possible in combination with beam-swing measurements. A direct measurement of the collision frequency, and subsequently the neutral wind, would lead to more accurate Joule heating rate measurements and allow for a better measurement-to-model comparison.

It should also be noted that the energy deposition by Joule heating strongly depends on the local position within the convection pattern (Foster et al., 1983). So additionally to the strength of the convection pattern, i.e. the electric fields and the ion velocities, the size and shape of the convection pattern is of high importance. Both, the *Heelis* and the *Weimer* convection model, have been shown to struggle with giving the accurate size of the convection pattern (Pokhotelov et al., 2008). One possible improvement might be the application of the *assimilative mapping of ionospheric electrodynamics* method to obtain the high-latitude plasma convection (Richmond & Kamide, 1988; Cousins et al., 2013; Pokhotelov et al., 2021).

6 Conclusion

It has been shown that EISCAT measurements and TIE-GCM simulations give similar variations of the Joule heating rate with respect to the Kp index, the Kan-Lee merging electric field E_{KL} and the magnetic local time. However, the variations are not equally strong in measurements and models and, therefore, the empirical scaling of Joule heating rates in TIE-GCM runs should be adjusted with respect to these parameters. Significant differences between TIE-GCM runs driven with the *Heelis* and *Weimer* convection models have been found and the scaling factor should be adjusted with respect to this as well. The measurement Joule heating rate changes drastically with magnetic local time with the largest heating rates in the midnight sector (for $Kp < 4$ and all E_{KL} values) and the dusk sector (for $Kp > 4$). While the model runs generally show the same trend, it can be seen that the required scaling factor is distinctly different for the investigated MagLT sectors. In conclusion, it has been shown that the choice of polar plasma convection model, the magnetic local time, and the geophysical conditions, i.e. the Kp index and the Kan-Lee merging electric field, impact the required scaling factor. The seasonal dependence of the required scaling factor cannot be determined with the current measurement dataset. Applying the adjusted scaling factor f found in our study would bring the Joule heating rate estimation by the TIE-GCM model closer to the EISCAT measurements.

For future investigations, extending the dataset to sufficiently cover all seasons is crucial. The current gaps in the dataset are due to the fact that only certain measurements with the EISCAT ISR, i.e. *CP2* campaigns, can be applied to derive Joule heating rates. The upcoming EISCAT_3D system (McCrea et al., 2015) will be a major advance as the phased-array concept allows for multi-beam measurements and therefore does not require the rotation of a large radar dish. The EISCAT_3D radar will allow to create a large database suitable for the derivation of Joule heating rates within a short time of operation. Another advantage of phased-array multi-beam experiments is the possibility to perform pulse-to-pulse beam steering or software beam forming to collect data from many different beam directions without the need to mechanically steer the beam. Since all radar beams are available at nearly the same time, the time resolution of 3D ion velocity vectors will be the same as for the other ISR plasma parameters.

Open Research Section

Acknowledgments

EISCAT is an international association supported by research organisations in China (CRIRP), Finland (SA), Japan (NIPR and ISEE), Norway (NFR), Sweden (VR), and the United Kingdom (UKRI). The TIE-GCM and related Thermosphere-Ionosphere models have been developed by the "Atmosphere Ionosphere Magnetosphere" (AIM) Section of the

High Altitude Observatory (HAO) at NCAR (see http://www.hao.ucar.edu/modeling/tgcm). The TIE-GCM data was generated on the 'Kratos' High-Performance Data Analysis Cluster (HPDA) at the German Aerospace Center (DLR) Jena. Gunter Stober is a member of the Oeschger Center for Climate Change Research (OCCR). Huixin Liu acknowledges supports by JSPS grants 17KK0095, 18H01270, 20H00197, 22K21345. This work is carried out at Kyushu University with the support of the SCOSTEP SVS program and the JSPS PBASE program.

References

Alken, P., Thébault, E., Beggan, C. D., Amit, H., Aubert, J., Baerenzung, J., ... Zhou, B. (2021, December). International Geomagnetic Reference Field: the thirteenth generation. *Earth, Planets and Space*, *73*(1), 49. doi: 10.1186/s40623-020-01288-x

Baloukidis, D., Sarris, T. E., Tourgaidis, S., Pirnaris, P. I., Aikio, A. T., Virtanen, I. I., ... Papadakis, K. (2023, April). A comparative assessment of the distribution of Joule heating in altitude as estimated in TIE-GCM and EISCAT over one solar cycle. *ESS Open Archive eprints*, *808*, essoar.168056818. doi: 10.22541/essoar.168056818.80893950/v1

Barraclough, D. R. (1988, April). IAGA Division I Working Group 1: International Geomagnetic Reference Field revision 1987. *Geophysical Journal International*, *93*(1), 187-189. doi: 10.1111/j.1365-246X.1988.tb01397.x

Baumjohann, W., & Treumann, R. A. (1996). *Basic space plasma physics*. Imperial College Press. doi: 10.1142/p015

Brekke, A., Doupnik, J. R., & Banks, P. M. (1973, December). A preliminary study of the neutral wind in the auroral E region. *Journal of Geophysiscal Research*, *78*(34), 8235-8250. doi: 10.1029/JA078i034p08235

Brekke, A., & Kamide, Y. (1996, March). On the relationship between Joule and frictional heating in the polar ionosphere. *Journal of Atmospheric and Terrestrial Physics*, *58*(1), 139-143. doi: 10.1016/0021-9169(95)00025-9

Codrescu, M. V., Fuller-Rowell, T. J., & Foster, J. C. (1995, September). On the importance of E-field variability for Joule heating in the high-latitude thermosphere. *Geophysical Research Letters*, *22*(17), 2393-2396. doi: 10.1029/95GL01909

Cousins, E. D. P., Matsuo, T., & Richmond, A. D. (2013, December). SuperDARN assimilative mapping. *Journal of Geophysical Research (Space Physics)*, *118*(12), 7954-7962. doi: 10.1002/2013JA019321

Deng, Y., Maute, A., Richmond, A. D., & Roble, R. G. (2009, April). Impact of electric field variability on Joule heating and thermospheric temperature and density. , *36*(8), L08105. doi: 10.1029/2008GL036916

Deng, Y., & Ridley, A. J. (2007, September). Possible reasons for underestimating Joule heating in global models: E field variability, spatial resolution, and vertical velocity. *Journal of Geophysical Research (Space Physics)*, *112*(A9), A09308. doi: 10.1029/2006JA012006

Emery, B. a., Lathuillere, C., Richards, P. G., Roble, R. G., Buonsanto, M. J., Knipp, D. J., ... Niciejewski, R. (1999, February). Time dependent thermospheric neutral response to the 2-11 November 1993 storm period. *Journal of Atmospheric and Solar-Terrestrial Physics*, *61*(3-4), 329-350. doi: 10.1016/S1364-6826(98)00137-0

Folkestad, K., Hagfors, T., & Westerlund, S. (1983, December). EISCAT: An updated description of technical characteristics and operational capabilities. *Radio Science*, *18*(6), 867-879. doi: 10.1029/RS018i006p00867

Foster, J. C., St. -Maurice, J. P., & Abreu, V. J. (1983, June). Joule heating at high latitudes. *Journal of Geophysical Research*, *88*(A6), 4885-4897. doi: 10.1029/JA088iA06p04885

Grassmann, V. (1993, April). An incoherent scatter experiment for the measurement of particle collisions. *Journal of Atmospheric and Terrestrial Physics*, *55*(4-5), 573-576. doi: 10.1016/0021-9169(93)90006-K

Günzkofer, F., Pokhotelov, D., Stober, G., Liu, H., Liu, H. L., Mitchell, N. J., ... Borries, C. (2022, October). Determining the Origin of Tidal Oscillations in the Ionospheric Transition Region With EISCAT Radar and Global Simulation Data. *Journal of Geophysical Research (Space Physics)*, *127*(10), e2022JA030861. doi: 10.1029/2022JA030861

Günzkofer, F., Liu, H., Stober, G., Pokhotelov, D., & Borries, C. (2023, November). *[Dataset] Evaluation of the Empirical Scaling Factor of Joule Heating Rates in TIE-GCM with EISCAT Measurements.* Zenodo. doi: 10.5281/zenodo.10162944

Heelis, R. A., Lowell, J. K., & Spiro, R. W. (1982, August). A model of the high-latitude ionospheric convection pattern. *Journal of Geophysical Research*, *87*(A8), 6339-6345. doi: 10.1029/JA087iA08p06339

Huang, Y., Richmond, A. D., Deng, Y., & Roble, R. (2012, August). Height distribution of Joule heating and its influence on the thermosphere. *Journal of Geophysical Research (Space Physics)*, *117*(A8), A08334. doi: 10.1029/2012JA017885

Kan, J. R., & Lee, L. C. (1979, July). Energy coupling function and solar wind-magnetosphere dynamo. *Geophysical Research Letters*, *6*(7), 577-580. doi: 10.1029/GL006i007p00577

Kavanagh, A. J., Ogawa, Y., & Woodfield, E. E. (2022, June). Two Techniques for Determining F-Region Ion Velocities at Meso-Scales: Differences and Impacts on Joule Heating. *Journal of Geophysical Research (Space Physics)*, *127*(6), e30062. doi: 10.1029/2021JA030062

Kelley, M. C. (2009). *The Earth's Ionosphere: Plasma Physics and Electrodynamics, Second Edition.* Elsevier Academic Press.

Laundal, K. M., & Richmond, A. D. (2017, March). Magnetic Coordinate Systems. , *206*(1-4), 27-59. doi: 10.1007/s11214-016-0275-y

Maute, A. (2017, October). Thermosphere-Ionosphere-Electrodynamics General Circulation Model for the Ionospheric Connection Explorer: TIEGCM-ICON. , *212*(1-2), 523-551. doi: 10.1007/s11214-017-0330-3

McCrea, I., Aikio, A., Alfonsi, L., Belova, E., Buchert, S., Clilverd, M., ... Vierinen, J. (2015, December). The science case for the EISCAT_3D radar. *Progress in Earth and Planetary Science*, *2*, 21. doi: 10.1186/s40645-015-0051-8

Nicolls, M. J., Bahcivan, H., Häggström, I., & Rietveld, M. (2014, December). Direct measurement of lower thermospheric neutral density using multifrequency incoherent scattering. *Geophysical Research Letters*, *41*(23), 8147-8154. doi: 10.1002/2014GL062204

Nozawa, S., Ogawa, Y., Oyama, S., Fujiwara, H., Tsuda, T., Brekke, A., ... Fujii, R. (2010, August). Tidal waves in the polar lower thermosphere observed using the EISCAT long run data set obtained in September 2005. *Journal of Geophysical Research (Space Physics)*, *115*(A8), A08312. doi: 10.1029/2009JA015237

Nygrén, T., Aikio, A. T., Kuula, R., & Voiculescu, M. (2011, May). Electric fields and neutral winds from monostatic incoherent scatter measurements by means of stochastic inversion. *Journal of Geophysical Research (Space Physics)*, *116*(A5), A05305. doi: 10.1029/2010JA016347

Palmroth, M., Janhunen, P., Pulkkinen, T. I., Aksnes, A., Lu, G., Østgaard, N., ... Germany, G. A. (2005, September). Assessment of ionospheric Joule heating by GUMICS-4 MHD simulation, AMIE, and satellite-based statistics: towards a synthesis. *Annales Geophysicae*, *23*(6), 2051-2068. doi: 10.5194/angeo-23-2051-2005

Pokhotelov, D., Fernandez-Gomez, I., & Borries, C. (2021, September). Polar tongue

of ionisation during geomagnetic superstorm. *Annales Geophysicae*, *39*(5), 833-847. doi: 10.5194/angeo-39-833-2021

Pokhotelov, D., Mitchell, C. N., Spencer, P. S. J., Hairston, M. R., & Heelis, R. A. (2008, March). Ionospheric storm time dynamics as seen by GPS tomography and in situ spacecraft observations. *Journal of Geophysical Research (Space Physics)*, *113*(A3), A00A16. doi: 10.1029/2008JA013109

Rich, F. J., Gussenhoven, M. S., Hardy, D. A., & Holeman, E. (1991, April). Average height-integrated Joule heating rates and magnetic deflection vectors due to field-aligned currents during sunspot minimum. *Journal of Atmospheric and Terrestrial Physics*, *53*, 293-308. doi: 10.1016/0021-9169(91)90113-L

Richmond, A. D., & Kamide, Y. (1988, June). Mapping electrodynamic features of the high-latitude ionosphere from localized observations: Technique. , *93*(A6), 5741-5759. doi: 10.1029/JA093iA06p05741

Richmond, A. D., Ridley, E. C., & Roble, R. G. (1992, March). A thermosphere/ionosphere general circulation model with coupled electrodynamics. *Geophysical Research Letters*, *19*(6), 601-604. doi: 10.1029/92GL00401

Rodger, A. S., Wells, G. D., Moffett, R. J., & Bailey, G. J. (2001, January). The variability of Joule heating, and its effects on the ionosphere and thermosphere. *Annales Geophysicae*, *19*(7), 773-781. doi: 10.5194/angeo-19-773-2001

Schunk, R., & Nagy, A. (2009). *Ionospheres: Physics, Plasma Physics, and Chemistry*. Cambridge Academic Press. doi: 10.1017/CBO9780511635342

Thayer, J. P. (1998, January). Height-resolved Joule heating rates in the high-latitude E region and the influence of neutral winds. *Journal of Geophysical Research*, *103*(A1), 471-487. doi: 10.1029/97JA02536

Thayer, J. P. (2000, October). High-latitude currents and their energy exchange with the ionosphere-thermosphere system. *Journal of Geophysical Research*, *105*(A10), 23015-23024. doi: 10.1029/1999JA000409

Tjulin, A. (2021). *Eiscat experiments* (Tech. Rep.). EISCAT Scientific Association. Retrieved from https://eiscat.se/wp-content/uploads/2021/03/Experiments_v20210302.pdf

Vickrey, J. F., Vondrak, R. R., & Matthews, S. J. (1982, July). Energy deposition by precipitating particles and Joule dissipation in the auroral ionosphere. *Journal of Geophysical Research*, *87*(A7), 5184-5196. doi: 10.1029/JA087iA07p05184

Weimer, D. R. (1995, October). Models of high-latitude electric potentials derived with a least error fit of spherical harmonic coefficients. *Journal of Geophysical Research*, *100*(A10), 19595-19608. doi: 10.1029/95JA01755

Weimer, D. R. (2005, May). Improved ionospheric electrodynamic models and application to calculating Joule heating rates. *Journal of Geophysical Research (Space Physics)*, *110*(A5), A05306. doi: 10.1029/2004JA010884